Journal of Power Sources 577 (2023) 233149

Contents lists available at ScienceDirect

Journal of Power Sources

journal homepage: www.elsevier.com/locate/jpowsour

Thermal transport in lithium-ion batteries: The effect of degradation

Lena Spitthoff [a,*], Markus Solberg Wahl [a], Preben J.S. Vie [a,b], Odne Stokke Burheim [a]

[a] Department of Energy and Process Engineering, Norwegian University of Science and Technology (NTNU), Trondheim, NO-7491, Norway
[b] Institute for Energy Technology (IFE), NO-2027, Kjeller, Norway

HIGHLIGHTS

- A reduction in thermal conductivity of up to 65% compared to BoL.
- Operating conditions have a significant impact on the thermal conductivity.
- The CCC reduced by 50% from BoL to a SoH of 70 to 75%.

ARTICLE INFO

Keywords:
Lithium-ion batteries
Thermal conductivity
Cell cooling coefficient

ABSTRACT

In this work, we report thermal conductivities of pristine and degraded electrodes, from commercial lithium-ion batteries. The thermal conductivities were measured with and without electrolyte solvent and at different compaction pressures. The effect of degradation on thermal transport, both internal and external, is assessed. In addition, the overall cell cooling efficiency is reported as a function of the state-of-health, and full cell thermal conductivities are estimated. A reduction of the electrode thermal conductivity of up to 65% is found for degraded material. The reduction appears to be the most extreme for dry graphite anodes. Both mechanical clamping of the cells during cycling, and cold temperatures, appear to mitigate the reduction in thermal conductivity. The cell cooling efficiency is found to decrease by 50% at a state-of-health of 70–75%. Decreased wetting, due to a reduction in the amount of electrolyte and gassing, is believed to be responsible for the discrepancy between cell cooling efficiency and thermal conductivity of the electrodes. The main cause of a reduction in full cell thermal conductivity was found to be due to a reduction in anode thermal conductivity and reduction of electrolyte solvent.

1. Introduction

The transition to electric vehicles powered by lithium-ion batteries (LiBs) as well as stationary storage supporting wind and solar energy has emerged as one of the most important elements in reducing the world's CO_2 emissions [1,2]. Compared to internal combustion engines, the environmental footprint of LiBs is mainly associated with the production phase [3,4]. To reduce the environmental impact, the production must therefore be improved, as well as the lifespan of the batteries that are produced [1,5] (see Table 1).

Temperature is an important parameter that affects energy efficiency, performance and the lifespan of LiBs [6–10]. The lifespan of a battery has been found to be one of the most significant factors to determine its life cycle cost, where a doubling of the life reduces the carbon footprint by 23% and the life cycle cost by 33% [10]. Both high and low temperatures have been found to accelerate the degradation of LiBs, where low temperature causes increased lithium plating during charging and high-temperature i.a. increases the rate of solid electrolyte interface (SEI) growth [11]. A detailed understanding and an optimized thermal management system (TMS) are therefore of high importance, as they will not only allow to prolong the life of the batteries [12] but also allow the design of a TMS that meets the demands of a cell throughout its entire lifetime.

In many situations, high power and fast charging or discharging rates are required, which typically generates large amounts of heat [13]. It has been found that the most effective method of cooling a battery is surface cooling, i.e. through the side-faces of a pouch cell, either in contact with cooling blocks, by immersion cooling or convective air cooling [14]. In general, liquid cooling systems are more effective than air-based systems, although heavier and more complex [14,15]. One of the main drawbacks of surface cooling pouch cells is that it generates layer-to-layer non-uniformities with regard to cycling temperature, which has been found to reduce the performance and lifetime of the cells [16,17]. In addition, the directionality of thermal gradients has been shown to dictate diverging and non-uniform

* Corresponding author.
E-mail address: burheim@ntnu.no (L. Spitthoff).

https://doi.org/10.1016/j.jpowsour.2023.233149
Received 7 February 2023; Received in revised form 21 April 2023; Accepted 1 May 2023
Available online 31 May 2023

Table 1
List of abbreviations, subscripts and superscripts.

BoL	Beginning of Life
CCC	Cell Cooling Coefficient
EoL	End of Life
k	Thermal conductivity
LiB	Lithium-ion Battery
SEI	Solid Electrolyte Interface
SoC	State of Charge
SoH	State of Health
TMS	Thermal Management System
Superscript	
$\perp$	Through-plane
eff	Effective full cell
64 Ah	Material extracted from the 64 Ah NMC532/graphite cell
6.55 Ah	Material extracted from 6.55 Ah LCO/graphite cell
Subscript	
BoL	Material extracted at BoL
MC	Material extracted at EoL, Cell was mechanical clamped during cycling
No MC	Material extracted at EoL, Cell was not mechanical clamped during cycling
Low T	Material extracted at EoL, Cell was cycled at 5 °C
High T	Material extracted at EoL, Cell was cycled at 45 °C
W,top	Material extracted at EoL, Cell was water-cooled from the top, material extracted from the centre of the cell
W,mid	Material extracted at EoL, Cell was water-cooled from the top, material extracted from the centre of the cell
W,bottom	Material extracted at EoL, Cell was water-cooled from the top, material extracted from the centre of the cell

degradation modes [18]. The main alternative to pouch cooling is removing the generated heat through the tabs. While a thermal gradient is required to transfer heat, it is important to minimize it [6]. Due to the high thermal conductivity of the current collectors, tab cooling is therefore believed to give smaller thermal gradients if the cell and its cooling system are designed appropriately, and hence result in a more uniform current density [17,19].

What is ultimately important when dimensioning a cooling system, is how efficiently the heat can be removed. This depends on the external cooling of the battery, as well as the heat transport inside the battery. The heat transport inside the battery is defined by the effective thermal conductivity of the full cell. Thermal conductivities have been measured and reported either on material, electrode or full cell level [20,21]. On the material level, thermal conductivities have been measured at different stages: fresh material prior to being implemented into a cell and therefore before formation and any contact with the electrolyte, or extracted from a cell at BoL or after degradation. The full-cell thermal conductivity ($k_{eff,\perp}$) is either calculated from the material thermal conductivities or measured at the full-cell level.

In 2020, Wei et al. [22] reviewed thermal conductivities for cathode materials considering the dependency on temperature and the volume fraction of active material. Steinhardt et al. [21] published a meta-analysis in 2022 on the experimental results of thermal conductivity in LiB available in literature both on material and full cell level. But neither Wei et al. nor Steinhardt et al. differentiated if measurements have been done before or after formation. Murashko et al. [23] and Steinhardt et al. [24] conducted thermal conductivity measurements on full LiB cells, investigating the dependency on temperature. Steinhardt et al. also considered different external compression pressure. Tendera et al. [20] analysed the effect of geometry and operation (e.g. SoC, temperature, pressure) on the thermal conductivity of full LiBs. Richter et al. [25] also conducted thermal conductivity measurements on a hard carbon anode and NMC cathode from one commercial LiB, considering different external compression pressure, as well as comparing values from a cell at beginning of life (BoL) versus end of life (EoL). They only noticed a slight increase in the thermal conductivity of the NMC cathode while the hard carbon anode showed no change with degradation.

In addition, there are several approaches using modelling to investigate the effect of the electrode microstructure on the thermal conductivity [26–29]. Werner et al. [30] combined experimental work and modelling to investigate the thermal conductivity of active materials and their effect on the thermal properties of full cells. The recent studies by Steinhardt et al. [21] and Tendera et al. [20] pointed out the need for further research on the effect of degradation on the material thermal conductivity on the battery state, especially the SoH. In addition, the difference in thermal conductivity for dry and soaked LiB material, *ergo* the degree of wetting, has been shown to be significant [25,31]. The effect of electrolyte degradation on the capacity retention is well known [32–34] and studies have shown decreased amounts of electrolyte solvent [35,36] as well as gassing [37] in degraded cells. However, there is currently little research published on quantifying the reduction in electrode wetting caused by electrolyte degradation. This is important as the actual thermal conductivity will be somewhere between the dry and the soaked values in degraded cells.

Measuring the cooling performance of the external cooling system can be challenging due to the many different and mostly complex cell chemistries and geometries. Hales et al. [19] therefore developed a method to measure the heat rejection from a cell, expressed by a single coefficient, the cell cooling coefficient (CCC), see Eq. (6). As the CCC is calculated based on non-destructive measurements, it is possible to monitor how the ability to reject heat changes for ageing cells. Dondelewski et al. [9] used the CCC to investigate the efficacy of surface and tab cooling, but without presenting how it changes for aged cells. Diaz et al. [38] on the other hand, use the same experimental set-up to study the dependency of heat generation of a cell on factors such as SoH, SoC, frequency and temperature without presenting the CCC.

Knowledge of thermal conductivity throughout the life of LiB allow to engineer a good TMS thought the entire lifetime of a cell. Temperature distributions within a LiB become more inhomogeneous for degraded cells and the difference between external temperature measurements and internal temperatures increase [39]. A lot of BMS use external temperature sensors for estimating battery temperature, in combination with virtual sensing to identify hot spots within a cell [40]. To allow for a good estimation, material thermal conductivities are needed. Material thermal conductivities at different states of battery health have barely been reported so far [20]. In this paper, we study the effect of degradation on the thermal conductivity of the electrode material (Sections 4.1–4.3) — specifically the effect of thermal management and mechanical clamping of the cells during cycling. Since the amount of electrolyte solvent is reduced in degraded cells, the thermal conductivities are also measured for both dry and electrolyte-soaked materials. Finally, we use the CCC method introduced by Hales et al. [19] for a holistic investigation of how the cell cooling properties change with degradation (Section 4.4) — ultimately studying the effect of changes in thermal conductivity on the cells cooling efficiency (Section 4.5). The exact thermal conductivities measured are included in the supplementary material to serve as a reference for future studies.

2. Theory and background

This section presents the general theory and background for thermal conductivity in LiBs. Factors influencing thermal conductivity on the material (Section 2.1.1) and cell level (Section 2.1.2) are discussed. A brief overview of thermal conductivity values reported in the literature is also presented, with a special focus on which phase of the battery's lifetime the electrode was extracted from. Lastly, the CCC method is introduced (Section 2.3).

2.1. Influencing factors

2.1.1. Material level

Lodges et al. [41] divided the physical aspects influencing thermal conductivity into three categories:

- Composition
- Morphology (i.e. porosity, particle size distribution and particle shape).
- Thickness ratio of coating to current collector.

The composition of active material sets the maximum thermal conductivity, which can be achieved.

To estimate the thermal conductivity of the full cell, a general model has been established. The Krischer model [42] allows the modelling of two-phase porous components as a combination of the liquid and solid phases. Werner et al. [30] adapted this further to account for the presence of binder and carbon black leading to a continuous solid phase. It can be expressed with the following set of equations, where f_a is a weighting factor that depicts a kind of tortuosity and ϵ is the solid phase porosity.

$$k_{two-phase} = \left(\frac{f_a}{k_\perp} + \frac{f_a - 1}{k_\parallel}\right)^{-1} \tag{1}$$

$$k_\perp = \left(\frac{\epsilon}{k_{fluid}} + \frac{1-\epsilon}{k_{solid}}\right)^{-1} \tag{2}$$

$$k_\parallel = \epsilon k_{fluid} + (1-\epsilon)k_{solid} \tag{3}$$

Werner et al. [30] show that both solid materials exhibit a significantly higher thermal conductivity than the electrolyte-saturated porous matrix. Therefore, highly porous structures are expected to have lower thermal conductivity than electrodes with high solid content. As the thermal contact resistances between particles limit the global thermal conductivity, the particle–particle interface is of great importance. This is affected by the shape of the particles, the binder content and distribution and the manufacturing process, which includes coating, drying and calendering of the electrodes. Reported experimental values show large differences between dry and soaked measurements as well as a strong correlation between the pressure applied during the experiments [25,31]. The electrolyte provides better conductivity since it fills the voids in the pore structure. This facilitates heat transmission, even though the thermal conductivity of the electrolyte is small (between 0.45 and 0.6 W/mK [43,44]).

The thickness ratio of coating to current collector essentially determines the through-plane and in-plane thermal conductivity of double-sided electrodes [41]. The through-plane thermal conductivity can be calculated based on a serial connection of the thermal conductivities of the current collector (cc) and electrode coating (c).

$$k_\perp = (2d_c + d_{cc})\left(2\frac{d_c}{k_{\text{eff},c}} + \frac{d_{cc}}{k_{cc}}\right)^{-1} \tag{4}$$

2.1.2. Cell level

The through-plane thermal conductivity of the full cell can either be measured directly or calculated from the material thermal conductivity and thermal contact resistance using Eq. (5):

$$k_{\text{eff}} = \frac{\sum d_i}{\sum R_i + \sum \frac{d_i}{k_i}} \tag{5}$$

Different parametric effects have been investigated in the literature on the full cell level. Recent publications by Tendera et al. [20] and Steinhardt et al. [21] have reviewed and investigated effects such as cell format, chemistry, compaction pressure, temperature and SoC. The effect of the cell format appears not too obvious but cylindrical cells tend to have lower thermal conductivities. Cells with NMC cathodes tend to have higher thermal conductivities, and cells with LFP cathodes have rather small thermal conductivities. The capacity appears to have no effect. Compaction pressure increases thermal conductivity but the extent varies between studies. In general, the relationship with the measurement temperature appears to be negative. The relationship is rather strong for cells with an LCO cathode. Tendera et al. [20] show a change of 10% in thermal conductivity when the measurement temperature is varied by 45 °C for a larger set of commercial NMC–graphite cells. It was not possible to establish a clear SoC-dependency on the thermal conductivity. The dependencies that were determined are rather weak and vary between linear, parabolic and no relationship at all. There are not many studies reporting on the correlation between SoH and $k_\perp$. Vertiz et al. [45] report a reduction in thermal conductivity of 29% for an aged LFP/graphite pouch cell (SoH < 80%) compared to BoL. Kovachev et al. [46] investigated the effect of mechanical clamping during degradation cycling on the changes in thermal conductivity of the full cell for a commercial NMC/graphite pouch cell. They found a decrease in thermal conductivity of around 23% for the cell cycled without any clamping (80% SoH), while the thermal conductivity was only reduced by 3% and 4% when a pretension was applied (0.56 MPa and 0.06 MPa, respectively). Kovachev et al. explained the SoH dependence of $k_\perp$ with an additional thermal resistance on the anode side caused by the SEI growth. They also assume that electrolyte consumption and gas development due to the electrolyte reduction could have led to a decrease in $k_\perp$.

Formation. During the manufacturing process, LiBs run through several steps that potentially affect the thermal conductivity of the LiB. This process includes three major parts: electrode preparation, cell assembly, and electrochemical activation. The focus of this study is on electrochemical activation: the formation and ageing. The electrochemical activation steps are applied to enable operation stability. The purpose is to enable a stable solid-electrolyte interface (SEI) layer to prevent the irreversible consumption of electrolytes and allow for sufficient electrolyte wetting [47]. There are different protocols for this process steps but commonly they consist of several charge and discharge cycles starting at low rates (e.g., C/10 or C/20) and only low voltages (e.g., 1.5 V) with a gradual increase in both, and rest sessions in between. After or during formation cycles, the cells are stored for complete electrolyte wetting and SEI stabilization — the so-called ageing step. The gas generated during the formation and ageing is removed and the cells are resealed. Studies measuring the thermal conductivity of a full battery, do this after the electrochemical activation. Studies measuring the thermal conductivity of electrodes usually do this in two different steps. Either the material is measured before it is assembled into a battery (① in Fig. 1), or the material is measured after extracting it from a full cell ② i.e. after electrochemical activation.

Degradation. Battery degradation is known to be a result of several simultaneous physicochemical processes: these processes lead to loss of Li inventory (LLI), loss of active materials (LAM), and impedance increase due to reaction kinetics degradation. LLI is mainly caused by the growth and decomposition of the SEI layer, electrolyte decomposition, and Li plating and dendrite formation. LAM can be introduced by the dissolution of material, structural degradation, particle isolation, corrosion of the current collector, loss of electric contact and electrode delamination. Increased impedance is a result of the formation of passive films at the active particle surfaces, pore-clogging, as well as electrolyte conductivity losses and loss of electric contact [13]. Based on the physical influence factors on $k_\perp$ discussed in Section 2.1.1, we know the $k_\perp$ can be affected by changes in the thermal conductivity of the solid phase, the fluid phase, porosity and tortuosity, and the layer thickness. The thermal conductivity of the solid phase could be affected by Li-plating, SEI growth or changes in the microstructure. The thermal conductivity of the liquid phase of a full battery can be affected by electrolyte consumption, reduction and gassing. As we measure the electrode material after extracting it from the cell, changes in the measured thermal conductivity are not due to the liquid phase. But measuring the electrode material both dry and soaked allows us to analyse this effect in general. The porosity and tortuosity of the cell can also be affected.

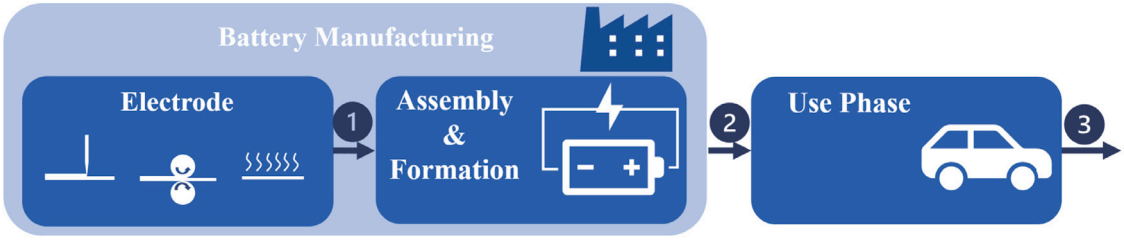

Fig. 1. Schematic of LiB manufacturing processes and the measurement points — (1) prior to formation, (2) extracted from cell at BoL, (3) at EoL.

Table 2
Measured thermal conductivities of porous electrodes — soaked with electrolyte (s) and dry (d). All electrodes do not contain any current collector foil. Average particle size (PS) and porosity (ϵ) are specified when available.

Material	T [K]	p [bar]	$k_{\perp,d}$ [W/mK]	$k_{\perp,s}$ [W/mK]	Life stage	Other	Ref.
NMC	296	2.3	0.30 ± 0.05	0.82 ± 0.06	BoL		[48]
NMC	–	–		0.83	BoL		[49]
NMC	298	–		0.66	BoL	$\epsilon = 0.191$	[50]
NMC	296	2.3	0.14 ± 0.02	0.54 ± 0.02	BoL		[51]
NMC	296	2.3	0.18 ± 0.01	0.52 ± 0.06	58% SoH		[51]
LCO	–	–		1.58	–		[43]
LCO	295	9.3	0.36 ± 0.03	1.10 ± 0.06	fresh	PS=19 μm	[52]
LCO	296	2.3	0.17 ± 0.02	1.03 ± 0.09	fresh		[48]
Graphite	296	2.3	0.832 ± 0.03	0.89 ± 0.01	BoL		[48]
Graphite	296	2.3	0.26 ± 0.01	1.11 ± 0.02	fresh		[48]
Graphite	295	9.3	0.30 ± 0.01	0.89 ± 0.04	fresh	PS=45 μm	[52]
Carbon cones	295	9.3	0.07 ± 0.01	0.36 ± 0.01	fresh	PS=0.5–4 μm	[52]
Carbon cones	295	9.3	0.41 ± 0.02	1.26 ± 0.07	fresh	PS=0.5–4 μm	[52]
Graphite	298	–		1.45	BoL	$\epsilon = 0.308$	[50]
Graphite	–	–		1.44	BoL		[49]
hard carbon	296	2.3	0.31 ± 0.05	0.66 ± 0.06	BoL		[51]
hard carbon	296	2.3	0.33 ± 0.01	0.6 ± 0.02	58% SoH		[51]

2.2. Thermal conductivities

Table 2 presents measured thermal conductivities of LCO and NMC cathodes, and porous graphite anodes, both soaked in electrolyte solvent and dry. The life stage is specified when available. *Fresh* refers to material that was never introduced into a LiB. In general, the value range is quite wide going from 0.36 to 1.45 W/mK for soaked carbon-based anodes, 0.54 to 0.82 W/mK for soaked NMC cathodes and 1.03 to 1.58 W/mK for LCO cathodes. There is no obvious trend comparing fresh and BoL material, but it has to be noted that it was never the same material measured both fresh and extracted from a cell. A direct comparison is therefore not possible. This will be discussed in more detail in Sections 4.2 and 2.1.2.

2.3. Overall thermal transport: Cell cooling coefficient

To analyse and compare the amount and rate at which heat that can be removed from a battery, the heat generation, the geometry of the cell and cooling system, and relevant material properties must be taken into account. The CCC method offers a non-destructive way of describing the ability of a cell to reject heat with a single number [19], the cooling efficiency. It, therefore, enables characterization as a function of e.g., SoC, SoH, temperature. The method relies on generating heat in the cell itself, which is done with alternating positive and negative current pulses. This keeps the cell at a constant SoC during the experiment.

The CCC is defined as the amount of heat that can be transferred from the cell ($\dot{Q}_{tot}$), relative to the temperature difference between the cooled part and the hottest side of the cell (ΔT_{cell}) [19]:

$$CCC = \frac{\dot{Q}_{tot}}{\Delta T_{cell}}. \tag{6}$$

The CCC rig used to measure the heat given off by the cells is illustrated in Fig. 2(a). The surface-cooled setup is a good approximation to commonly used cooling systems in the automotive industry, where two cells are stacked together with cooling on each side [53,54]. The numbers show the location of K-type thermocouple temperature sensors and the underlined numbers indicate sensors located on the backside of the cell. The setup was encapsulated in styrofoam insulation. This was done in order to prevent additional pathways for the generated heat other than through the cooled surface.

The cells were cooled with Grant LT ecocool 100 circulating water baths set at 25 °C. The operating temperature of each cell was therefore dependent on the efficiency of the cooling configuration. The average temperature difference between the top and bottom of the cell is used.

The known thermal conductivity (k) of the aluminium fins shown in Fig. 2 enables calculation of the transferred heat ($\dot{Q}$) through fin i as

$$\dot{Q}_i = \frac{k}{l_i} A_i \Delta T_i, \tag{7}$$

where A_i is the cross-sectional area of the fin, and l_i is the distance between two temperature sensors with a temperature difference ΔT_i. The total heat transferred by the four fins therefore becomes

$$\dot{Q}_{tot} = \sum_{i=1}^{4} \dot{Q}_i. \tag{8}$$

The CCCs versus time calculated using Eq. (6) for one cell at different SoHs are shown in Fig. 2(b). Further information about the CCC method can be found in the papers by Hales et al. [16,19].

3. Experimental

Section 3.1 presents the cells the electrodes were extracted from as well as the formation and degradation process the cells went through. Section 3.2 briefly introduces the thermal conductivity meter and the settings used for the thermal conductivity measurements. Section 3.3 specifies the experimental details of the CCC measurement.

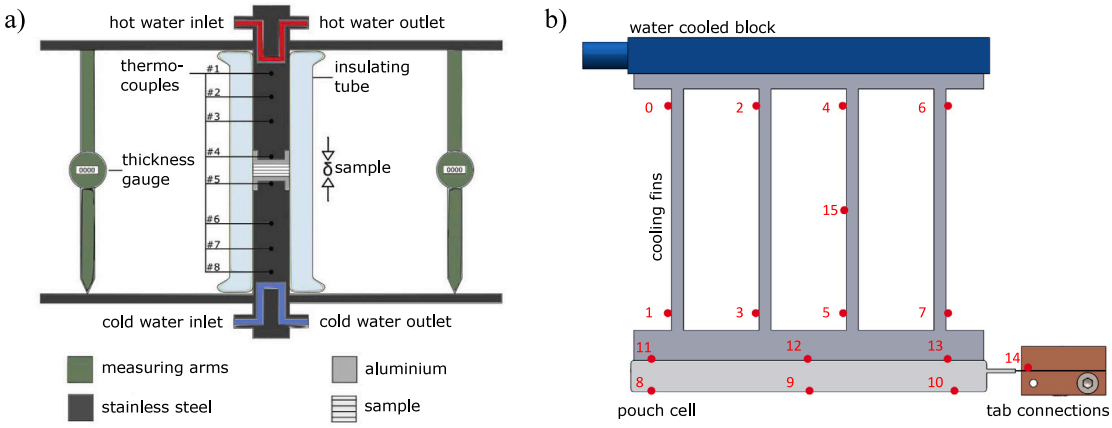

Fig. 2. Schematic of the rig used for measuring the thermal conductivity (**a**) reprinted from [31], and CCC setup (**b**) adapted from [55], showing the cell, the cooling blocks, the cooling fins, the copper tab connections and the temperature sensor placement.

3.1. Electrode material

The electrode materials investigated in this study were extracted from three different LiB. The first cell is a 10 Ah NMC622/Graphite cell, the second cell is a 64 Ah NMC532/Graphite cell and the third cell is a 6.55 Ah LCO/Graphite cell. The first cell was investigated as part of studying the effect of formation on thermal conductivity (Section 3.1.1). For this, both fresh electrode material and full LiB were obtained from the manufacturer. The second and third cell types were part of investigating the effect of degradation (Section 3.1.2). More detailed information on the cell types, formation and degradation conditions follow in the respective sections.

3.1.1. Formation

We studied the effect of the formation cycling on the thermal conductivity of electrode material. For the investigations, electrodes free of electrolyte and electrochemically untreated (① in Fig. 1) are compared to electrodes extracted from ready-to-use pouch cells (covered with electrolyte and undergone the formation, (② in Fig. 1). This was done for material from two cells with similar specifications e.g. NMC622/graphite pouch cells from CustomCell. The anode material was artificial graphite (4 mAh/cm^2) and the cathode was NCM622 (3.5 mAh/cm^2). The pouch cell underwent 2x C/10 and 2x C/5 at room temperature of 25 °C for the formation and 2x C/5 at room temperature of 20 °C for a check-up in the voltage window 3.0 up to 4.2 V. The electrolyte used is: EC:DMC (50:50) $LiPF_6$ with vinylene carbonate (VC).

3.1.2. Degradation study

Table 3 summarizes the cell cycling conditions used for the degradation study. The electrode materials were extracted from these cells as described in Section 3.1.3. The first cell type used in this study is the LG Chem JP3 64 Ah pouch cell with an NMC532 cathode and graphite anode. The degradation study using this cell type investigates the effect of mechanical clamping during degradation cycling. All cells were cycled inside a temperature chamber at 25 °C. This cell type was cycled either with or without being clamped. This was obtained by fixing the pouch cells between two 1 cm thick aluminium plates and secured with 6 bolts. Each bolt was fixed with a 1 Nm torque and kept in this position, effectively limiting the swelling otherwise seen for degraded cells.

The second cell type used in this study is a 6.55 Ah pouch cell from Shenzhen Melasta Battery Co with an LCO cathode and graphite anode. The electrolyte is EC:EMC:DMC LiPF6 with VC and PC. As Table 3 specifies, the degradation study using Melasta cells focuses on different cooling strategies. Here the cells are either air-cooled within a temperature chamber at a specified temperature or water-cooled. The water cooling is detailed in Section 2.3. All cells have been charged with constant current, constant voltage charge and constant current discharge. The cycling was done within the full SoC window with voltage limits of 3 V and 4.2 V. The C rates and ambient temperatures as well as SOH are specified in Table 3. The electrode material of both cell types was extracted at BoL (② in Fig. 1) and EoL (③ in Fig. 1).

3.1.3. Materials harvesting

The disassembly of the battery cell and extraction of electrode material was done after fully discharging the battery. The cell was opened inside a glove box with an argon atmosphere. The electrodes were cleaned using DMC to remove the $LiPF_6$ salt. The materials were then dried inside the glovebox for at least 72 h and under vacuum for 15 min before measuring the thermal conductivity. The cleaning procedure was found to remove some electrode material and the thickness was therefore measured both prior to and after cleaning. The electrode material was extracted from random locations in the cells, excluding the very outer layers. When location-specific effects were investigated, the exact location from which the material was extracted will be specified.

3.2. Thermal conductivity rig

The thermal conductivity meter used in this work is presented and explained by Richter et al. [31] and Burheim et al. [56]. In summary, a constant heat flux is applied over a sample using a cold and warm water bath and the resulting temperature drop is measured. The thermal resistance obtained this way is plotted versus sample thickness to obtain the thermal conductivity.

The temperature of the heating bath was kept constant at 35 °C while the cooling bath was kept at 10 °C resulting in a sample temperature around room temperature. Measurements were carried out at compaction pressures of 2.0 bar, 2.9 bar, 3.9 bar, 4.8 bar, 5.8 bar and 6.0 bar. When measuring electrolyte solvent-soaked samples, materials were soaked in diethyl carbonate (DEC) for 30 min prior to the measurement.

Strict stability conditions for the heat flux and pressure were implemented that had to be met prior to proceeding with the measurement. This is to ensure accuracy and repeatability in the measured thermal conductivities, which was confirmed by repeated measurements on different samples from single cells.

Table 3
Conditions during degradation study (cooling temperature (T_{cool}), C rate, MC/no MC (MC: mechanical clamping)) and cell condition when electrodes were extracted (e.g FEC, SOH, thickness increase).

Cell type	Condition	T_{cool} [°C]	C rate	FEC	SOH [%]	d%	Electrode	Location	Label
64 Ah, pouch	BoL	–	–		100	100	Graphite		$C^{BoL}_{64\ Ah}$
							NMC		$NMC^{BoL}_{64\ Ah}$
	MC	25	1.5	2764	80.6	100	Graphite		C^{MC}_{64Ah}
							NMC		NMC^{MC}_{64Ah}
	no MC	25	0.75	1090	70.5	155	Graphite		C^{noMC}_{64Ah}
							NMC		NMC^{noMC}_{64Ah}
6.55 Ah, pouch	BoL	–	–		100	100	Graphite		$C^{BoL}_{6.55\ Ah}$
							LCO		$LCO^{BoL}_{6.55\ Ah}$
	low T	5	2	239	67	121	Graphite		$C^{lowT}_{6.55Ah}$
							LCO		$LCO^{lowT}_{6.55Ah}$
	high T	45	1	331	71	150	Graphite		$C^{highT}_{6.55Ah}$
	water-cooling	24	3	1024	73	135	Graphite	top	$C^{w;top}_{6.55Ah}$
							Graphite	centre	$C^{w;mid}_{6.55Ah}$
							Graphite	bottom	$C^{w;bottom}_{6.55Ah}$

3.3. CCC measurement procedure

The theory explaining the CCC method is presented in Section 2.3. The CCC tests were performed every 200 cycles or 10% drop in SoH, and always at 50% state of charge (SoC). To mitigate a shift in SoC, alternating positive and negative current pulses (4.5 C) were used to generate heat. The CCC was found to be independent of C-rate, see *Fig. 2* in the SI. The highest current was therefore chosen, as this gave the most stable measurements due to a larger denominator in Eq. (6). The pulse rate was 0.25 Hz, which was maintained for 3.6 h to ensure stable temperatures. The cells were left to rest for two hours between each characterization period. Multiple characterization periods were used to improve accuracy and to determine if the method itself caused degradation.

3.4. Uncertainty analysis

The errors presented for the thermal conductivity measurement values are the double standard deviation resulting from the linear regression. It has to be noted that there is an additional systematic error of 3% due to the rig set-up and calibration procedure. This is mainly due to the precision in temperature difference between the thermocouples. The error of the estimated effective thermal conductivities were calculated using error propagation:

$$s_a^2 = \sum_{i=1}^{n} \left(\frac{\delta f(x_1, x_2, x_3, \ldots, x_i)}{\delta x_i} s_{x_i} \right)^2 \quad (9)$$

4. Results and discussion

Results of the thermal conductivity measurements, the effect of degradation on changes in thermal conductivity and the cooling efficiency of LiBs are examined in the following sections. Section 4.1 analyses the influence of pressure and the presence of electrolyte solvent at BoL, Section 4.2 deals with the effect of formation, while Section 4.3 focuses on the effect of degradation on thermal conductivity and the effect of mechanical clamping, the temperature during duty cycling and local differences. Finally, we present the changes in CCC (Section 4.4) and effective full-cell thermal conductivities (Section 4.5) in an attempt to link the cooling efficiency with the thermal conductivities. All numeric values are included in the SI.

4.1. Thermal conductivity at BoL

This section presents the measured thermal conductivities as functions of pressure, as well as the impact of solvent at BoL. Results from earlier publications by Richter et al. [48] for similar electrodes harvested at BoL are included in the figures and depicted in grey.

4.1.1. Effect of pressure

Thermal conductivities of the dry electrode materials as a function of pressure are presented in Fig. 3(a). For the materials measured in this study, the graphite anodes show larger thermal conductivities than the cathodes, with large pressure dependencies. $C^{BoL}_{64\ Ah}$ shows the largest thermal conductivity (0.90 ± 0.02 W/mK at 2 bar), which increases by approximately 30% when the pressure is increased from 2 to 6 bar. The $C^{BoL}_{6.55\ Ah}$ shows an increase of 60% from 0.448 ± 0.018 W/mK in the same pressure range. The thermal conductivities of $NMC^{BoL}_{64\ Ah}$ (0.495 ± 0.003 W/mK at 2 bar) and $LCO^{BoL}_{6.55\ Ah}$ (0.272 ± 0.003 W/mK at 2 bar) increase by 13% and 19%, respectively.

When the electrodes are soaked in electrolyte solvent (Fig. 3(b)), the measured thermal conductivity is significantly higher than for the dry samples. In general, the pressure dependency also appears to be lower, both relative and in absolute value. The $C^{BoL}_{64\ Ah}$ shows a very large thermal conductivity of 1.93 ± 0.06 W/mK at 2 bar, which is significantly larger than both the $C^{BoL}_{6.55\ Ah}$ (1.27 ± 0.04 W/mK at 2 bar) and literature values for soaked graphite anodes reported by other studies (0.35 W/mK to 1.45 W/mK, summarized in Table 2). Repeated measurements confirmed the higher thermal conductivity of $C^{BoL}_{64\ Ah}$. Loges et al. [41] pointed out that the composition of active material sets the maximum thermal conductivity that can be achieved. In addition, the intrinsic thermal conductivity of graphite is strongly influenced both by the manufacturing process and the precise type of material as well as the orientation of the graphite. It can be as large as approx. 2000 W/mK [57]. Unfortunately, no details on the manufacturing process or the material composition were available for this commercial cell. The combination of binder and active material particles with the used manufacturing process is likely to allow for good particle–particle contact.

Compared to the dry measurements, the pressure dependency for the soaked anodes is very low, with an increase of 11% to 15% when increasing the pressure from 2 to 6 bar. The soaked $NCM^{BoL}_{64\ Ah}$ has a thermal conductivity of 1.03 ± 0.04 W/mK and the soaked $LCO^{BoL}_{6.55\ Ah}$ has a thermal conductivity of 0.919 ± 0.008 W/mK at 2 bar. This is in the range of thermal conductivities reported in the literature for soaked NMC cathodes (0.52 to 0.83 W/mK, Table 2) and soaked

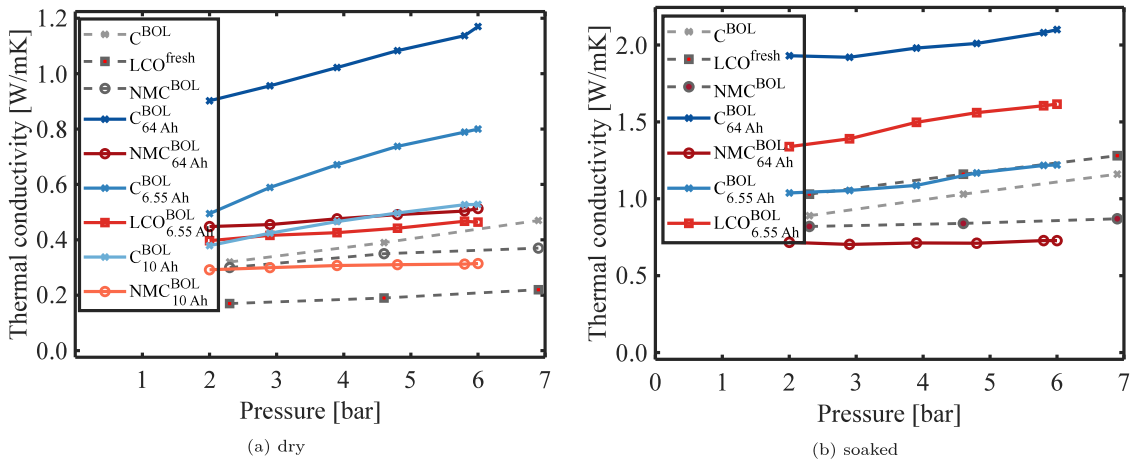

Fig. 3. Thermal conductivity of electrode materials at BoL. Data depicted in grey from Richter et al. [48].

LCO cathodes (1.0 to 1.58 W/mK, Table 2). $NMC^{BoL}_{64\ Ah}$ barely shows any change with pressure increase (approx. 1%), while the pressure dependency of $LCO^{BoL}_{6.55\ Ah}$ is similar to the dry values (22% increase with the increase in pressure from 2 to 6 bar).

The dependence of thermal conductivity on pressure could be explained by uneven surfaces and porosity, producing voids in the measurement volume as well as thermal resistance between particles. These effects become less significant when the sample is soaked, as the electrolyte solvent fills these voids. This is discussed in more detail in the next section.

4.1.2. Effect of electrolyte

The results presented in Section 4.1.1 already showed a large increase in thermal conductivity due to the presence of electrolyte solvent. Fig. 4 presents the ratio of dry thermal conductivity and soaked thermal conductivity. The smaller the ratio, the more affected is the thermal conductivity by the presence of a solvent. A ratio of 1 would refer to the same thermal conductivity of dry and soaked material. $LCO^{BoL}_{6.55\ Ah}$ appears to be affected the most, with the dry value being only about 25% of the soaked. $NMC^{BoL}_{64\ Ah}$, on the other hand, is the least affected — the dry value is still about 60 to 70%. The graphite anodes have the same ratio at 2 bar, but the ratio is varying more with pressure for $C^{BoL}_{6.55\ Ah}$.

Whereas the effect of soaking slightly decreases for higher pressures in the JP3 cathode, the LCO cathode shows close to no effect of the increased pressure. Both graphite anodes are around 50% at 2 bar, the difference becoming smaller with increased pressure. $C^{BoL}_{6.55\ Ah}$ shows the largest pressure dependency, caused by the large pressure dependency of the dry electrodes.

When going from 2 bar to 6 bar, the thickness of the active material is reduced the most for $C^{BoL}_{6.55\ Ah}$ (2%), followed by 1.4% for both $NMC^{BoL}_{64\ Ah}$ and $C^{BoL}_{64\ Ah}$. $LCO^{BoL}_{6.55\ Ah}$ is the least compressed (0.6%). This is in agreement with the pressure dependency of the ratio (largest for $C^{BoL}_{6.55\ Ah}$, smallest for $LCO^{BoL}_{6.55\ Ah}$). Although the compression may not change the porosity of the material drastically, it can increase the particle–particle contact substantially. Another reasonable explanation could be a difference in particle size distribution. The particle size distribution affects the area of the solid–gas interphase (dry) and solid–liquid interphase (soaked) and therefore the thermal interfacial resistance. The thermal interfacial resistance over the solid–liquid interphase (also known as Kapitza resistance) has been shown to decrease with an increasing wetting coefficient [58]. Therefore, for different particle size distributions, the ratio between the dry and soaked thermal conductivity varies.

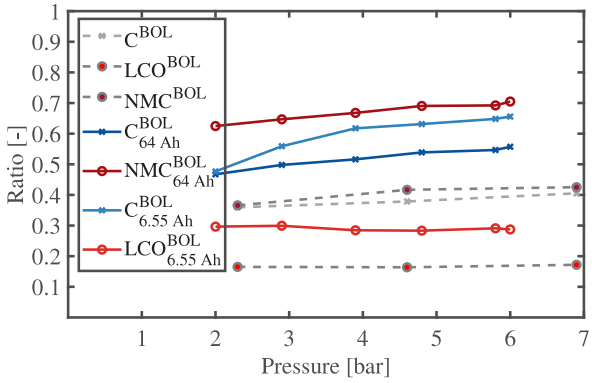

Fig. 4. Ratio of dry thermal conductivity to soaked thermal conductivity at BoL. Data depicted in grey from Richter et al. [48].

Table 4
Thermal conductivities at 2 bar measured fresh (e.g. prior to introducing into the cell) and at BoL.

	Fresh $k_{am,d}$	BoL $k_{am,d}$
Graphite	0.407 ± 0.002	0.379 ± 0.008
NMC622	0.32 ± 0.05	0.29 ± 0.03

4.2. Effect of formation

Table 4 presents the thermal conductivities prior to and after electrochemical activation. In general, it appears that the thermal conductivities of the electrodes extracted from the cells after they went through the electrochemical formation are smaller than the thermal conductivity of electrodes that were never implemented in a cell (fresh). However, there is quite some variation in the reduction. The thermal conductivity of the dry graphite anode is reduced by 7%, whereas the dry thermal conductivity of the NMC cathode is reduced by 9%. Possible reasons for the changes in thermal conductivity have been discussed in Section 2.1.2, e.g. porosity changes due to gassing, and the formation of SEI on both anode and cathode. This can affect the thermal interface resistance between particles, between particles and solvent and between particles and gas.

4.3. Thermal conductivity of degraded electrodes

Fig. 5 presents the change in thermal conductivity compared to the same material at BoL. The values are here averaged for all applied pressures, and for the 6.55 Ah cell also for different thermal management

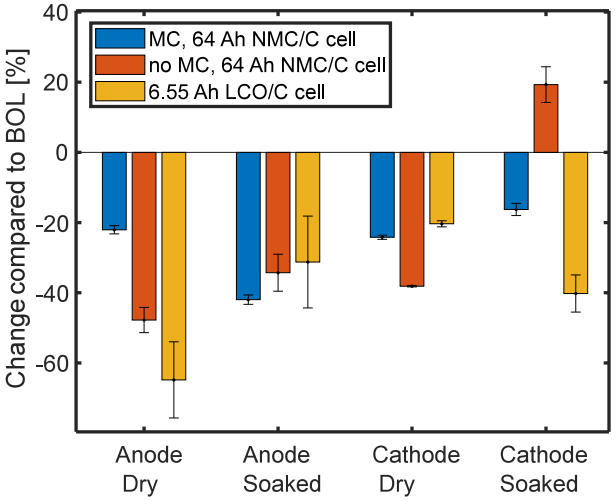

Fig. 5. Change in thermal conductivity compared to BoL, averaged over all pressure steps and operation conditions. (MC: Mechanical Clamping). (For interpretation of the references to colour in this figure legend, the reader is referred to the web version of this article.)

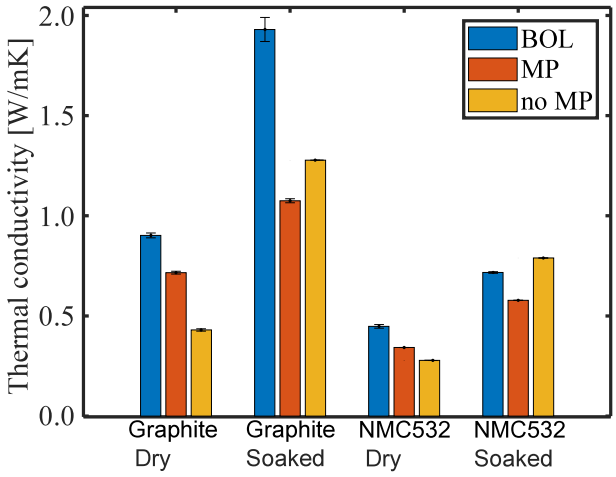

Fig. 6. Effect of clamping during cycling on the thermal conductivity of the 64 Ah NMC532/Graphite cell. (Labels $C_{64\ Ah}$ and $NMC_{64\ Ah}$ in Table 2, MC: Mechanical Clamping).

Table 5
Compressibility: Relative thickness changes when pressure is increased from 2 to 6 bar, JP3.

	NMC cathode	Graphite anode
BoL	−1.103 ± 0.0011%	−1.34 ± 0.07%
MC	−0.680 ± 0.0005%	−0.61 ± 0.08%
no MC	−0.937 ± 0.0008%	−4.63 ± 0.09%

strategies during cycling. This results in large standard deviations but it merely aims to get a brief overview of the changes before discussing the impact of clamping (Section 4.3.1), the effect of thermal management (Section 4.3.2) and local differences (Section 4.3.3) in more detail. All degraded electrodes have a significantly lower thermal conductivity compared to BoL, both soaked and dry, and for all cycling conditions. The only exception is the soaked $NMC_{64\ Ah}^{noMC}$, which appears to have a higher thermal conductivity when aged. Generally, the anode appears to be more affected than the cathode and the dry more than the soaked. The most extreme drop in thermal conductivity is observed for the dry $C_{6.55\ Ah}^{EoL}$, around 60%. It has to be noted, that there are cell-to-cell variations in the SoH (see Table 3) which is also likely to factor into the differences between the thermal conductivities of the degraded material.

For the measurement, the electrodes are harvested from degraded cells and are cleaned and soaked in solvent. Both the BoL and degraded material are soaked in the same way. In a full battery cell, on the other hand, this may not be representable. While at BoL, assuming fully soaked electrode values appear fair, it might be less so at EoL due to gassing and thickness volume changes. When considering the values for calculating the effective thermal conductivity of a degraded LiB, the dry and soaked values should therefore be seen as a lower and upper limit.

4.3.1. Effect of clamping during degradation

Fig. 6 presents the thermal conductivities of the anode and cathode extracted from the 64 Ah cell at 2 bar, at BoL and EoL. We compare the thermal conductivity of material extracted from a cell that was cycled with mechanical clamping (MC, orange) and a cell that was cycled without applied clamping (no MC, yellow). All dry measurements show a decrease in thermal conductivity at EoL compared to BoL. When the cells were not clamped during cycling, the reduction in thermal conductivity is more extreme, most extreme for the anode (51%, 38% for the cathode).

When mechanical clamping of the cells was applied during cycling, a similar reduction for both electrodes of around 22% is observed. Considering the soaked electrode measurements, the effect of clamping during cycling on the thermal conductivity is reversed. For the anode, there is still a significant reduction observable (43% MC, 28% no MC). The thermal conductivity is still decreased compared to BoL for the material from the clamped cell (17%) but is increased for the cathode from the unclamped cell. *Ergo*, the same material shows a reduction of 38% when measured dry and an increase of 17% when measured soaked (compared to the dry and soaked thermal conductivity at BoL, respectively).

Possible reasons for the differences in thermal conductivity could be due to changes in particle–particle contact due to particle cracking resulting from volume changes. This is considered to benefit from adding pressure [59,60]. This is also likely to suppress micro-gassing which affects the porosity. This hypothesis is supported by the observed changes in the thickness and compressibility of the material. A thickness increase for both electrodes compared to BoL was observed. The anode showed an extreme thickness increase and large variations (37 ± 20%) when not clamped during cycling (compared to 25 ± 3% when clamped). One reason for the large variations in the cells without clamping is that the active material was partially stuck on the separator when opening the cell. The cathode thickness increase is very similar for MC (6%) and no MC (7%). Another observation is the change in compressibility of the electrode material (Table 5). The compressibility of the material (2 bar to 6 bar) is similar for the anode and cathode at BoL (1.3% and 1.1%, respectively) and is reduced for all degraded cathode material and the anode material with MC. The compressibility of the degraded anode material of the unclamped cell on the other hand increased significantly to 4.7%. Based on those observations it appears reasonable to assume that a combination of porosity and structural changes is causing these effects. Another aspect could be an increased resistance between the active material and the current collector. The effective thermal conductivity of the current collector double-coated with active material is measured and Eq. (4) is used to estimate the thermal conductivity of the active material from this measured value. Any changes in thermal resistance between the current collector and active material would therefore be included in the thermal conductivity of the active material as presented and discussed. As the thickness of the electrodes increases and for the cells without clamping, the porosity appears to increase, it becomes apparent that at EoL a perfectly soaked electrode material is unlikely. This will be discussed in more detail in Section 4.5.

Table 6
Thermal conductivities of Melasta graphite anodes at 2 bar measured at BoL and EoL using different thermal management strategies during cycling degradation.

	$k_{e,d}$	$k_{am,d}$	$k_{e,s}$	$k_{am,s}$
$C^{BoL}_{6.55\ Ah}$	0.604 ± 0.003	0.495 ± 0.003	1.27 ± 0.04	1.04 ± 0.04
$C^{lowT}_{6.55\ Ah}$	0.321 ± 0.003	0.267 ± 0.003	1.02 ± 0.03	0.86 ± 0.03
$C^{highT}_{6.55\ Ah}$	0.204 ± 0.002	0.177 ± 0.002	0.663 ± 0.011	0.573 ± 0.011
$C^{w,mid}_{6.55\ Ah}$ (mod. T)	0.224 ± 0.004	0.193 ± 0.004	0.665 ± 0.008	0.581 ± 0.008
$LCO^{BoL}_{6.55\ Ah}$	0.470 ± 0.003	0.397 ± 0.003	1.584 ± 0.008	1.339 ± 0.008
$LCO^{lowT}_{6.55\ Ah}$	0.376 ± 0.003	0.318 ± 0.003	1.1066 ± 0.0018	0.9378 ± 0.0018

d — dry, s — soaked, e — electrode, am — active material.

Table 7
Thermal conductivities of Melasta graphite anodes at 6 bar measured at BoL and EoL using different thermal management strategies during cycling degradation.

	$k_{e,d}$	$k_{am,d}$	$k_{e,s}$	$k_{am,s}$
$C^{BoL}_{6.55\ Ah}$	0.976 ± 0.002	0.800 ± 0.002	1.49 ± 0.02	1.22 ± 0.02
$C^{lowT}_{6.55\ Ah}$	0.569 ± 0.003	0.474 ± 0.003	1.10 ± 0.16	0.93 ± 0.16
$C^{highT}_{6.55\ Ah}$	0.384 ± 0.002	0.333 ± 0.002	0.717 ± 0.002	0.620 ± 0.002
$C^{w,mid}_{6.55\ Ah}$	0.292 ± 0.005	0.251 ± 0.005	0.930 ± 0.004	0.813 ± 0.004
$LCO^{BoL}_{6.55\ Ah}$	0.5494 ± 0.0019	0.4644 ± 0.0019	1.910 ± 0.007	1.615 ± 0.007
$LCO^{lowT}_{6.55\ Ah}$	0.439 ± 0.005	0.372 ± 0.005	1.1405 ± 0.0016	0.9665 ± 0.0016

4.3.2. Effect of thermal management

This section describes the effect of different thermal management strategies (see Table 3) on the thermal conductivity of the Melasta electrodes measured at EoL. Tables 6 and 7 present the thermal conductivity of the anodes at BoL and EoL at 2 bar and 6 bar, respectively. $k_{e,d}$ and $k_{e,s}$ are the thermal conductivities (dry and soaked, respectively) of the electrode sheets, e.g. including the current collector. For $k_{am,d}$ and $k_{am,s}$, the contribution of the current collector has been calculated to estimate the isolated effect of the active material.

In general, the dry anode values appear to be affected the most by degradation. It also appears that the thermal conductivities of $C^{highT}_{6.55\ Ah}$ are affected more severely. The thermal conductivity of $C^{lowT}_{6.55\ Ah}$ was reduced by 46% (averaged over all pressure steps), while it was reduced by 63% and 67% when cycled at an ambient temperature of 45 °C ($C^{highT}_{6.55\ Ah}$) or one-side water-cooled with 25 °C ($C^{w,mid}_{6.55\ Ah}$), respectively. The thermal conductivity of the soaked materials is not as significantly reduced, but a similar trend is observed. An even stronger link to the temperature at which the cell was cycled becomes apparent. The thermal conductivity of $C^{lowT}_{6.55\ Ah}$ was reduced by 21% compared to BoL, for $C^{w,mid}_{6.55\ Ah}$ it was reduced by 37% and for $C^{highT}_{6.55\ Ah}$ it was reduced by 47%.

$LCO^{lowT}_{6.55\ Ah}$ also shows a reduction in thermal conductivity which is in a similar range as the respective anode. Although, here it behaves the opposite way in terms of solvent being present. The dry thermal conductivity is reduced by 20% while the soaked one is reduced by 40%.

4.3.3. Local differences

Fig. 7 presents the thermal conductivities of the cell cooled in the CCC setup presented in Fig. 7 (a). To study the location-dependent changes in thermal conductivity, we differentiate between thermal conductivity measurements of the 5 top layers on the cooling side (Top, $C^{w,top}_{6.55\ Ah}$), the 5 bottom layers on the insulated side (Bottom, $C^{w,bottom}_{6.55\ Ah}$), and 5 centre layers in the middle of the cell (Mid, $C^{w,mid}_{6.55\ Ah}$). The very outer layer was excluded on each side as even though it was coated from both sides, only one side is electrochemically active during cycling. At BoL a maximum cycling temperature of 34.1 °C on the insulated side and 29.8 °C on the cooling side were measured on the battery surface. The temperatures increased to 40.8 °C and 30.7 °C at the EoL, respectively.

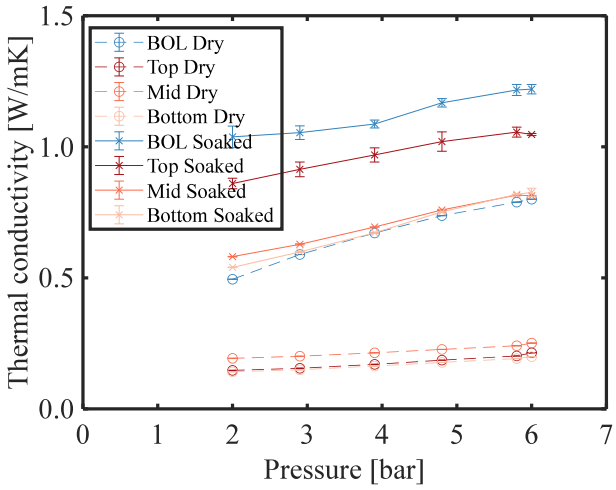

Fig. 7. Thermal conductivity at different locations for the water-cooled Melasta cell.

Table 8 presents the thermal conductivities of the different layers for both 2 bar and 6 bar as well as dry and soaked. In general, we observe significant differences in thermal conductivity based on the location of the electrodes that were extracted — especially when measured soaked. The thermal conductivity appears to be the lowest for the bottom layer, which is the insulated side that therefore experienced the highest cycling temperatures.

When measured dry, only minor differences due to the location can be observed. The top and bottom layers have very similar thermal conductivities and are reduced by 70 to 75% compared to BoL. The thermal conductivity of the mid layer is still the largest and reduced by about 60 to 69% compared to BoL. Interestingly, when soaked the thermal conductivities of the locations compare differently. Soaked, the thermal conductivities of the mid and bottom layers are nearly the same, about 32 to 48% smaller than at BoL. The thermal conductivity of the top layer is significantly larger, with only a reduction of about 11 to 17% compared to BoL. This is in agreement with the observations in Section 4.3.2 on the relationship between changes in thermal conductivity and cycling temperature as the thermal conductivity of the layers with the lowest temperature, decreases the least.

In Section 4.1, it was found that the pressure dependency for the anode at BoL decreased with soaking: increasing the pressure from 2 bar to 6 bar, the thermal conductivity increased by 62% for dry anodes but only 18% for soaked. For the top layer, a similar dependency on the pressure is observed although weaker (46% and 22%, respectively). For the mid- and bottom layers, it turned (mid: 30% and 40%, bottom: 41% and 53%). The compressibility is significantly larger for degraded material compared to BoL but the location has no significant effect. The higher compressibility suggests a higher porosity and crack density, and may explain the increased sensitivity to pressure for the thermal conductivities measured for degraded electrodes.

The visual inspection of the layers upon opening showed that both the layers towards the top and bottom of the cell appeared to be significantly more degraded and a quite substantial amount of active material came off when separating the layers. (SI, Fig. 4) . Measuring the layer thickness after opening and pre-washing showed the largest thickness increase for the top layer (35% ± 5%) and a similar thickness increase for the middle and bottom layer (26% ± 2%). It was noted that especially the top layer showed a large variation in thickness. During the washing and preparation of the electrodes for the measurement, a substantial loss of active material was noticed. This was the most extreme for the top layer. It was noted as a reduction of the thickness of about 11% for the top layers, 6% for the bottom layer, while no significant change was noted for the mid layer.

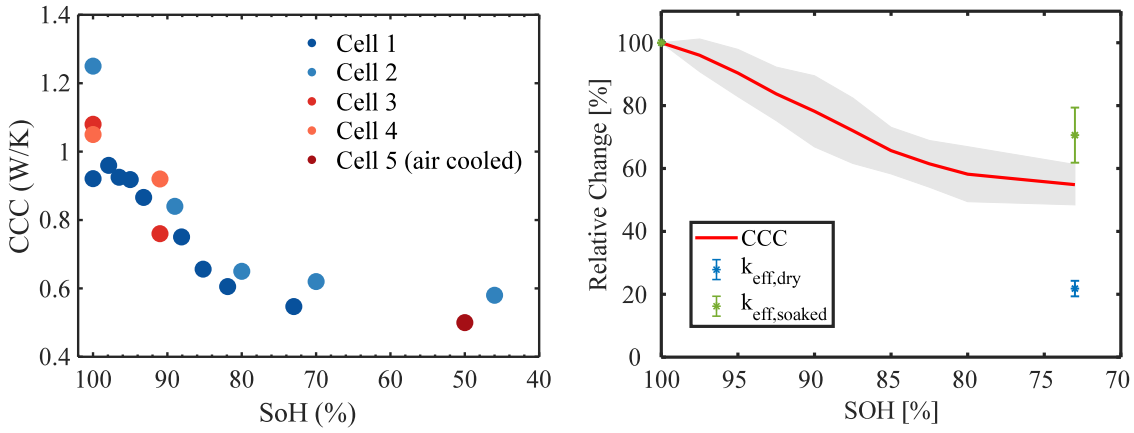

(a) CCC measurements (b) Relative change.

Fig. 8. CCC values and relative change of CCC and effective thermal conductivity as a function of SoH. Additional measurements from other cells that were available from other experiments are also included. The relative decrease in CCC is 50% at EoL for both the surface and tab-cooled cells, although the absolute reduction is larger with the pouch-cooled cells. Cells 2–5 reported in [55]. .

Table 8
Thermal conductivities for water-cooled cell at different locations.

	Dry		Soaked	
	2 bar	6 bar	2 bar	6 bar
$C^{BoL}_{6.55\ Ah}$	0.4947 ± 0.0006	0.8000 ± 0.0003	1.038 ± 0.040	1.220 ± 0.018
$C^{w,top}_{6.55\ Ah}$	0.147 ± 0.001	0.214 ± 0.001	0.860 ± 0.020	1.047 ± 0.004
$C^{w,mid}_{6.55\ Ah}$	0.193 ± 0.001	0.251 ± 0.001	0.581 ± 0.001	0.813 ± 0.0008
$C^{w,bottom}_{6.55\ Ah}$	0.1417 ± 0.0003	0.1991 ± 0.0007	0.540 ± 0.001	0.826 ± 0.016

4.4. The measured CCC values

To investigate how changes in the thermal conductivities of a single electrode affect the full cell, the CCC coefficients were measured for the 6.55 Ah LCO/Graphite pouch cell, as explained in Sections 2.3 and 3.3. Compared to the single electrodes, the CCC captures the overall effect of degradation on the thermal transport of the full cell, while also masking the direct cause of the changes observed.

All CCCs measured are summarized in Fig. 7(a), plotted as a function of SoH. All cells presented in this section are 6.55 Ah LCO/Graphite cells. Cell 1–4 were cooled with water cooling from one side, as described in Section 2.3. Cell 5 was cycled in a temperature chamber kept at 25 °C, e.g. air cooled. Cell 1 and 2 were cycled beyond 80% SoH, whereas the test was stopped at only 90% SoH for cell 3 and 4. From Fig. 7(a) it is seen how the cells' ability to transmit heat is reduced as the cells degrade, observed as a reduction in the CCC. The temperature difference required to transfer off a given amount of heat is therefore increased. It can be seen how the reduction in the CCC follows approximately the same trend for all cells. The cycled cells show CCC reductions of more than 50%, although from different starting points. It also appears that the largest change occurs before 80% SoH has been reached and that the decrease slows down as the cells age. The variations between the cells before cycling (100% SoH) can be due to production differences in the new cells [61], or due to variations in the experimental setup, e.g., the placement of the thermocouple temperature sensors. The electrodes used for the thermal conductivity measurements were taken from Cell 1 in Fig. 7(a), with samples taken from the outer layers at the top side (cooled) and the bottom (insulated), as well as from the middle.

4.5. Effective full cell thermal conductivities

The combination of electrode measurements and the CCCs enables the validity and actual effect of the electrode measurements to be assessed. Table 9 presents the estimated effective thermal conductivity of the full cells both at BoL and EoL. The effective thermal conductivity was estimated using Eq. (5). The EoL values are estimated using only the EoL values of the anode for the Melasta cell (unless specified otherwise) and the thermal conductivity of the anode and cathode at EoL for the JP3 cell, as well as including the measured thickness increase. Both thickness changes and thermal conductivity changes of other layers (e.g. current collector, separator, pouch laminate) are considered negligible. Although, when calculating the extreme case of a "dry-off", the thermal conductivities of the dry separator and dry cathode were used.

The relative values presented in this section are all in comparison to the effective thermal conductivity of the battery at BoL. The effective thermal conductivity at BoL was calculated using only soaked values, as it appears to be fair to assume all layers to be fully soaked at BoL. The full cell thermal conductivity at BoL is calculated to be 0.86 ± 0.08 W/mK for the JP3 cell and 0.94 ± 0.10 W/mK for the Melasta cell. This fits well within reported literature values for the cross-plane thermal conductivity of 0.284 W/mK to 1.63 W/mK for pouch cells [20]. Although, this is a very wide range — it can be said that the value of the JP3 cell compares well to the measurements by Tendera et all [20] of commercial NMC532 and graphite pouch cells measured at similar temperatures (0.81 to 1.03 W/mK).

Using the soaked values, a reduction of around 19% compared to BoL was calculated for 64 Ah NMC/Graphite cells that were clamped during the degradation study. On the other hand, the thermal conductivity of the 64 Ah cell that was not clamped appears to have not changed due to degradation. It is essential to point out, that when considering BoL cells it might be fair to assume the layers to be fully soaked — but it is less so when considering EoL. This becomes even clearer when considering that the cell without clamping increased in thickness by 55%. When considering the dry and soaked thermal conductivities as the extremes for the actual thermal conductivity of a full cell, the degradation will result in shifting the actual thermal conductivity from close to the soaked value in the direction of the dry value due to dry-off. Considering the dry values, a reduction of around 53% compared to BoL was calculated for 64 Ah cell that were clamped during the degradation study and 63% for the cells that were not clamped.

Considering the calculated thermal conductivity of the full 6.55 Ah LCO/Graphite cell, a reduction of 19% to 36% compared to BoL is observed. Using the dry values, the reduction would be as large as 75% to 80%. The reduction is the largest using the bottom values — the values from the side where the cell was insulated. This compares well with the observations from the CCC measurements. Fig. 7(b) visualizes

Table 9
Estimated effective through-plane thermal conductivities of the full cells at BoL and EoL.

	Effective thermal conductivity [W/mK]		Compared to BoL, S	
	Unit cell	Full battery	Unit cell	Full battery
BoL, dry	0.46 ± 0.04	0.46 ± 0.04		
BoL, soaked	0.90 ± 0.08	0.88 ± 0.08	100%	100%
MC, dry	0.41 ± 0.04	0.41 ± 0.04	45%	46%
MC, soaked	0.7 ± 0.1	0.7 ± 0.1	80%	81%
no MC, dry	0.32 ± 0.09	0.32 ± 0.09	35%	36%
no MC, soaked	0.89 ± 0.26	0.87 ± 0.25	99%	99%
BoL, dry	0.34 ± 0.04	0.33 ± 0.04		
BoL, soaked	1.04 ± 0.10	0.94 ± 0.10	100%	100%
W-C, top dry	0.19 ± 0.05	0.19 ± 0.05	18%	21%
W-C, top soaked	0.8 ± 0.2	0.75 ± 0.2	78%	81%
W-C, mid dry	0.23 ± 0.05	0.23 ± 0.05	22%	25%
W-C, mid soaked	0.67 ± 0.14	0.62 ± 0.13	64%	67%
W-C, bottom dry	0.19 ± 0.08	0.19 ± 0.08	18%	20%
W-C, bottom soaked	0.6 ± 0.2	0.6 ± 0.2	61%	64%
W-C, bottom dry (including cathode)	0.18 ± 0.08	0.18 ± 0.08	18%	20%
W-C, bottom soaked (including cathode)	0.6 ± 0.2	0.6 ± 0.2	58%	61%

Upper part: 64 Ah NMC532/Graphite pouch cell. Lower part: 6.55 Ah LCO/Graphite pouch cell. (W-C: water-cooled).

the relative changes in thermal conductivity and CCC compared to BoL values. The values presented are averaged for all respective measurements, depicted in the standard deviation. We recall that the CCC was reduced by 39% at EoL compared to BoL. This reduction is about 20%-points, 6%-points, and 3%-points (using only top, mid, and bottom values, respectively) larger than the reduction calculated based on the soaked thermal conductivity values. Again, degradation will result in shifting the actual thermal conductivity from close to the soaked value in the direction of the dry value due to dry-off. For this specific cell, an increase in cell thickness of 28% supports this claim. Including the measured changes in thermal conductivity for the LCO cathode, does not result in a significant further reduction. The dry reduction of the dry thermal conductivity is within the confidence interval, while the soaked value is reduced further by 3%-points. But in general, it can be said that the main reduction in the thermal conductivity of the full cell is due to changes in the anode and a reduction in the electrolyte solvent.

5. Conclusion

This work assessed the effect of degradation on thermal transport in LiB, both internal and external. The thermal conductivities of electrodes extracted from cells both at BoL and EoL were measured, as well as the overall CCC. The effective full-cell thermal conductivities were calculated, and the changes due to degradation were compared to measured changes in CCC. The main findings are:

- A reduction in thermal conductivity of up to 65% compared to BoL.
- The reduction in thermal conductivity is most extreme for dry graphite anodes.
- Clamping cells during cycling has the potential to mitigate the reduction in thermal conductivity.
- The thermal conductivity of graphite anodes cycled at cold temperatures appeared to reduce significantly less than when the cell was cycled at moderate or high temperatures.
- The CCC reduced by 50% from BoL to a SoH of 70 to 75%.

The effective full cell thermal conductivities were calculated using the measured thermal conductivities from the electrodes, separator and pouch laminate. Considering a fully soaked cell, k_{eff} was determined to be 0.86 ± 0.08 W/mK for the NMC/graphite cell and 0.94 ± 0.10 W/mK for the LCO/graphite cell at BoL. When assuming still a fully soaked cell at EoL, k_{eff} of the NMC/graphite cell was reduced by 19% when the cell was clamped during cycling and by 19 to 39% for the LCO/graphite cell. It is crucial to point out, that when considering BoL cells it might be fair to assume the layers to be fully soaked — but it is less so when considering the thickness increase of the full cell at EoL. When considering a full dry out of the cells at EoL, k_{eff} was reduced by 54% for the NMC/graphite cell when not clamped during cycling and up to 80% for the LCO/graphite cell. The actual thermal conductivity of the full cell is somewhere between those two extreme (dry and fully soaked) which was found to be in agreement with the CCC measurements. It was found that the main reduction in the thermal conductivity of the full cell is due to changes in the anode and a reduction in the electrolyte solvent.

CRediT authorship contribution statement

Lena Spitthoff: Conceptualization, Methodology, Formal analysis, Investigation, Writing – original draft, Writing – review and editing, Visualization. **Markus Solberg Wahl:** Methodology, Writing – original draft, Writing – review & editing. **Preben J.S. Vie:** Methodology, Writing – review & editing, Supervision. **Odne Stokke Burheim:** Conceptualization, Methodology, Writing – review & editing, Supervision.

Declaration of competing interest

The authors declare that they have no known competing financial interests or personal relationships that could have appeared to influence the work reported in this paper.

Data availability

Data will be made available on request.

Acknowledgements

The authors are grateful to Christian Helledal Trandem and Colin Ringdalen MacDonald for setting up the CCC rig and performing preliminary measurements. As well as, Omar Shagouri, Silvia Athisayamohan, Joachim Willumsen Grieg, Øyvind Storvik Ingebrigtsen and Emilie Rieber for help with the execution of the thermal conductivity measurements.

The authors would like to acknowledge the Research Council of Norway and partner companies of the BATTMAriNe project for financial support, grant number 281005.

The authors would like to acknowledge ENERSENSE funded by NTNU (Norwegian University of Science and Technology), Norway for financial support, grant number 68024013. All authors have read and agreed to the published version of the manuscript.

Appendix A. Supplementary data

Supplementary material related to this article can be found online at https://doi.org/10.1016/j.jpowsour.2023.233149.

References

[1] A. Opitz, P. Badami, L. Shen, K. Vignarooban, A.M. Kannan, Can Li-ion batteries be the panacea for automotive applications? Renew. Sustain. Energy Rev. 68 (April 2016) (2017) 685–692, http://dx.doi.org/10.1016/j.rser.2016.10.019.

[2] G. Zubi, R. Dufo-López, M. Carvalho, G. Pasaoglu, The lithium-ion battery: State of the art and future perspectives, Renew. Sustain. Energy Rev. 89 (April 2017) (2018) 292–308, http://dx.doi.org/10.1016/j.rser.2018.03.002.

[3] J.F. Peters, M. Baumann, B. Zimmermann, J. Braun, M. Weil, The environmental impact of Li-ion batteries and the role of key parameters – A review, Renew. Sustain. Energy Rev. 67 (2017) 491–506, http://dx.doi.org/10.1016/j.rser.2016.08.039.

[4] L.A.-W. Ellingsen, C.R. Hung, A.H. Strømman, Identifying key assumptions and differences in life cycle assessment studies of lithium-ion traction batteries with focus on greenhouse gas emissions, Transp. Res. D 55 (2017) 82–90, http://dx.doi.org/10.1016/j.trd.2017.06.028.

[5] B. Scrosati, J. Garche, Lithium batteries: Status, prospects and future, J. Power Sources 195 (9) (2010) 2419–2430, http://dx.doi.org/10.1016/j.jpowsour.2009.11.048.

[6] I.A. Hunt, Y. Zhao, Y. Patel, J. Offer, Surface cooling causes accelerated degradation compared to tab cooling for lithium-ion pouch cells, J. Electrochem. Soc. 163 (9) (2016) A1846–A1852, http://dx.doi.org/10.1149/2.0361609jes.

[7] J.S. Edge, S. O'Kane, R. Prosser, N.D. Kirkaldy, A.N. Patel, A. Hales, A. Ghosh, W. Ai, J. Chen, J. Jiang, S. Li, M.-C. Pang, L. Bravo Diaz, A. Tomaszewska, M.W. Marzook, K.N. Radhakrishnan, H. Wang, Y. Patel, B. Wu, G.J. Offer, Lithium ion battery degradation: What you need to know, Phys. Chem. Chem. Phys. (2021) 8200–8221, http://dx.doi.org/10.1039/d1cp00359c.

[8] C.R. Birkl, M.R. Roberts, E. Mcturk, P.G. Bruce, D.A. Howey, Degradation diagnostics for lithium ion cells, J. Power Sources 341 (2017) 373–386, http://dx.doi.org/10.1016/j.jpowsour.2016.12.011.

[9] O. Dondelewski, T. Szemberg O'Connor, Y. Zhao, I.A. Hunt, A. Holland, A. Hales, G.J. Offer, Y. Patel, The role of cell geometry when selecting tab or surface cooling to minimise cell degradation, ETransportation 5 (2020) 100073, http://dx.doi.org/10.1016/j.etran.2020.100073.

[10] L. Lander, E. Kallitsis, A. Hales, J.S. Edge, A. Korre, G. Offer, Cost and carbon footprint reduction of electric vehicle lithium-ion batteries through efficient thermal management, Appl. Energy 289 (January) (2021) 116737, http://dx.doi.org/10.1016/j.apenergy.2021.116737.

[11] T. Waldmann, M. Wilka, M. Kasper, M. Fleischhammer, M. Wohlfahrt-mehrens, Temperature dependent ageing mechanisms in lithium-ion batteries e a post-mortem study, J. Power Sources 262 (2014) 129–135, http://dx.doi.org/10.1016/j.jpowsour.2014.03.112.

[12] L.H. Raijmakers, D.L. Danilov, R.A. Eichel, P.H. Notten, A review on various temperature-indication methods for Li-ion batteries, Appl. Energy 240 (July 2018) (2019) 918–945, http://dx.doi.org/10.1016/j.apenergy.2019.02.078.

[13] L. Spitthoff, P.R. Shearing, O.S. Burheim, Temperature, ageing and thermal management of lithium-ion batteries, Energies 14 (5) (2021) 1248, http://dx.doi.org/10.3390/en14051248.

[14] D. Chen, J. Jiang, G.H. Kim, C. Yang, A. Pesaran, Comparison of different cooling methods for lithium ion battery cells, Appl. Therm. Eng. 94 (2016) 846–854, http://dx.doi.org/10.1016/j.applthermaleng.2015.10.015.

[15] Y. Zhao, L.B. Diaz, Y. Patel, T. Zhang, G.J. Offer, How to cool lithium ion batteries: Optimising cell design using a thermally coupled model, J. Electrochem. Soc. 166 (13) (2019) A2849–A2859, http://dx.doi.org/10.1149/2.0501913jes.

[16] A. Hales, M.W. Marzook, L. Bravo Diaz, Y. Patel, G. Offer, The surface cell cooling coefficient: A standard to define heat rejection from lithium ion battery pouch cells, J. Electrochem. Soc. 167 (2) (2020) 020524, http://dx.doi.org/10.1149/1945-7111/ab6985.

[17] G.M. Cavalheiro, T. Iriyama, G.J. Nelson, S. Huang, G. Zhang, Effects of nonuniform temperature distribution on degradation of lithium-ion batteries, J. Electrochem. Energy Convers. Storage 17 (2) (2020) 1–8, http://dx.doi.org/10.1115/1.4045205.

[18] R. Carter, T.A. Kingston, R.W. Atkinson III, M. Parmananda, M. Dubarry, C. Fear, P.P. Mukherjee, C.T. Love, Directionality of thermal gradients in lithium-ion batteries dictates diverging degradation modes, Cell Rep. Phys. Sci. (2021) 100351.

[19] A. Hales, L.B. Diaz, M.W. Marzook, Y. Zhao, Y. Patel, G. Offer, The cell cooling coefficient: A standard to define heat rejection from lithium-ion batteries, J. Electrochem. Soc. 166 (12) (2019) A2383–A2395, http://dx.doi.org/10.1149/2.0191912jes.

[20] L. Tendera, D. Wycisk, C. Gonzalez, G.K. Mertin, H. Pegel, K.P. Birke, Effects of geometric, structural and operational parameters on the thermal conductivity of lithium-ion cells, J. Power Sources 549 (2022) 232120.

[21] M. Steinhardt, J.V. Barreras, H. Ruan, B. Wu, G.J. Offer, A. Jossen, Meta-analysis of experimental results for heat capacity and thermal conductivity in lithium-ion batteries: A critical review, J. Power Sources 522 (2022) 230829.

[22] L. Wei, Z. Lu, F. Cao, L. Zhang, X. Yang, X. Yu, L. Jin, A comprehensive study on thermal conductivity of the lithium–ion battery, Int. J. Energy Res. 44 (12) (2020) 9466–9478, http://dx.doi.org/10.1002/er.5016.

[23] K.A. Murashko, J. Pyrhönen, J. Jokiniemi, Determination of the through-plane thermal conductivity and specific heat capacity of a Li-ion cylindrical cell, Int. J. Heat Mass Transfer 162 (6) (2020) 120330, http://dx.doi.org/10.1016/j.ijheatmasstransfer.2020.120330.

[24] M. Steinhardt, E.I. Gillich, M. Stiegler, A. Jossen, Thermal conductivity inside prismatic lithium-ion cells with dependencies on temperature and external compression pressure, J. Energy Storage 32 (2020) 101680, http://dx.doi.org/10.1016/j.est.2020.101680.

[25] F. Richter, P.J. Vie, S. Kjelstrup, O.S. Burheim, Measurements of ageing and thermal conductivity in a secondary NMC-hard carbon Li-ion battery and the impact on internal temperature profiles, Electrochim. Acta 250 (2017) 228–237, http://dx.doi.org/10.1016/j.electacta.2017.07.173.

[26] C. Sangrós, C. Schilde, A. Kwade, Effect of microstructure on thermal conduction within lithium-ion battery electrodes using discrete element method simulations, Energy Technol. 4 (12) (2016) 1611–1619, http://dx.doi.org/10.1002/ente.201600144.

[27] D. Oehler, P. Seegert, T. Wetzel, Modeling the thermal conductivity of porous electrodes of Li–Ion batteries as a function of microstructure parameters, Energy Technol. (2020) http://dx.doi.org/10.1002/ente.202000574.

[28] A. Vadakkepatt, B. Trembacki, S. Mathur, J. Murthy, Bruggeman's exponents for effective thermal conductivity of lithium-ion battery electrodes, J. Electrochem. Soc. 163 (2016).

[29] I. Sumirat, Y. Ando, S. Shimamura, Theoretical consideration of the effect of porosity on thermal conductivity of porous materials, J. Porous Materials 13 (3–4) (2006) 439–443, http://dx.doi.org/10.1007/s10934-006-8043-0.

[30] D. Werner, A. Loges, D.J. Becker, T. Wetzel, Thermal conductivity of Li-ion batteries and their electrode configurations – A novel combination of modelling and experimental approach, J. Power Sources 364 (2017) 72–83, http://dx.doi.org/10.1016/j.jpowsour.2017.07.105.

[31] F. Richter, S. Kjelstrup, P.J. Vie, O.S. Burheim, Thermal conductivity and internal temperature profiles of Li-ion secondary batteries, J. Power Sources 359 (2017) 592–600, http://dx.doi.org/10.1016/j.jpowsour.2017.05.045.

[32] P. Arora, R.E. White, M. Doyle, Capacity fade mechanisms and side reactions in lithium-ion batteries, J. Electrochem. Soc. 145 (10) (1998) 3647.

[33] M. Dubarry, N. Qin, P. Brooker, Calendar aging of commercial Li-ion cells of different chemistries – A review, Curr. Opin. Electrochem. 9 (2018) 106–113, http://dx.doi.org/10.1016/j.coelec.2018.05.023.

[34] R. Fang, P. Dong, H. Ge, J. Fu, Z. Li, J. Zhang, Capacity plunge of lithium-ion batteries induced by electrolyte drying-out: Experimental and modeling study, J. Energy Storage 42 (2021) 103013, http://dx.doi.org/10.1016/j.est.2021.103013.

[35] S. Lyu, N. Li, L. Sun, S. Jiao, H. Chen, W.-L. Song, Rapid operando gas monitor for commercial lithium ion batteries: Gas evolution and relation with electrode materials, J. Energy Chem. 72 (2022) 14–25, http://dx.doi.org/10.1016/j.jechem.2022.04.010.

[36] B. Rowden, N. Garcia-Araez, A review of gas evolution in lithium ion batteries, Energy Rep. 6 (2020) 10–18, http://dx.doi.org/10.1016/j.egyr.2020.02.022, 4th Annual CDT Conference in Energy Storage & Its Applications.

[37] W. Du, R.E. Owen, A. Jnawali, T.P. Neville, F. Iacoviello, Z. Zhang, S. Liatard, D.J. Brett, P.R. Shearing, In-situ X-ray tomographic imaging study of gas and structural evolution in a commercial Li-ion pouch cell, J. Power Sources 520 (2022) 230818.

[38] L.B. Diaz, A. Hales, M.W. Marzook, Y. Patel, G. Offer, Measuring irreversible heat generation in lithium-ion batteries: An experimental methodology, J. Electrochem. Soc. 169 (3) (2022) 030523.

[39] L. Spitthoff, M.S. Wahl, J.J. Lamb, P. Shearing, P. Vie, O.S. Burheim, On the relations between lithium-ion battery reaction entropy, surface temperatures and degradation, 2023, unpublished.

[40] A. Jinasena, L. Spitthoff, M.S. Wahl, J.J. Lamb, P.R. Shearing, A.H. Strømman, O.S. Burheim, Online internal temperature sensors in lithium-ion batteries: State-of-the-art and future trends, Front. Chem. Eng. 4 (2022) 6.

[41] A. Loges, S. Herberger, D. Werner, T. Wetzel, Thermal characterization of Li-ion cell electrodes by photothermal deflection spectroscopy, J. Power Sources 325 (2016) 104–115.

[42] O. Krischer, K. Kröll, Die Wissenschaftlichen Grundlagen Der Trocknungstechnik, Springer-Verlag, 2013.

[43] S. Chen, C. Wan, Y. Wang, Thermal analysis of lithium-ion batteries, J. Power Sources 140 (1) (2005) 111–124.

[44] G. Guo, B. Long, B. Cheng, S. Zhou, P. Xu, B. Cao, Three-dimensional thermal finite element modeling of lithium-ion battery in thermal abuse application, J. Power Sources 195 (8) (2010) 2393–2398.

[45] G. Vertiz, M. Oyarbide, H. Macicior, O. Miguel, I. Cantero, P.F. De Arroiabe, I. Ulacia, Thermal characterization of large size lithium-ion pouch cell based on 1d electro-thermal model, J. Power Sources 272 (2014) 476–484.

[46] G. Kovachev, A. Astner, G. Gstrein, L. Aiello, J. Hemmer, W. Sinz, C. Ellersdorfer, Thermal conductivity in aged Li-ion cells under various compression conditions and state-of-charge, Batteries 7 (3) (2021) 42.
[47] D.L. Wood, J. Li, S.J. An, Formation challenges of lithium-ion battery manufacturing, Joule 3 (12) (2019) 2884–2888.
[48] F. Richter, P.J. Vie, S. Kjelstrup, O.S. Burheim, Measurements of ageing and thermal conductivity in a secondary NMC-hard carbon Li-ion battery and the impact on internal temperature profiles, Electrochim. Acta 250 (2017) 228–237, http://dx.doi.org/10.1016/j.electacta.2017.07.173.
[49] S.D. Lubner, S. Kaur, Y. Fu, V. Battaglia, R.S. Prasher, Identification and characterization of the dominant thermal resistance in lithium-ion batteries using operando 3-omega sensors, J. Appl. Phys. 127 (10) (2020) 105104.
[50] G. Liebig, U. Kirstein, S. Geißendörfer, F. Schuldt, C. Agert, The impact of environmental factors on the thermal characteristic of a lithium–ion battery, Batteries 6 (1) (2020) 3.
[51] F. Richter, S. Kjelstrup, P.J. Vie, O.S. Burheim, Thermal conductivity and internal temperature profiles of Li-ion secondary batteries, J. Power Sources 359 (2017) 592–600, http://dx.doi.org/10.1016/j.jpowsour.2017.05.045.
[52] O.S. Burheim, M.A. Onsrud, J.G. Pharoah, F. Vullum-Bruer, P.J. Vie, Thermal conductivity, heat sources and temperature profiles of Li-ion batteries, ECS Trans. 58 (48) (2014) 145.
[53] L. Jin, P. Lee, X. Kong, Y. Fan, S. Chou, Ultra-thin minichannel LCP for EV battery thermal management, Appl. Energy 113 (C) (2014) 1786–1794, http://dx.doi.org/10.1016/j.apenergy.2013.07.013.
[54] Y. Huo, Z. Rao, X. Liu, J. Zhao, Investigation of power battery thermal management by using mini-channel cold plate, Energy Convers. Manage. 89 (2015) 387–395, http://dx.doi.org/10.1016/j.enconman.2014.10.015.
[55] C.R. MacDonald, C.H. Trandem, Impact of cooling methods on ageing in lithium-ion battery cells, 2021, NTNU, URL https://hdl.handle.net/11250/2824272.
[56] O. Burheim, P. Vie, J.G. Pharoah, S. Kjelstrup, Ex situ measurements of through-plane thermal conductivities in a polymer electrolyte fuel cell, J. Power Sources 195 (1) (2010) 249–256, http://dx.doi.org/10.1016/j.jpowsour.2009.06.077.
[57] C. Ho, R. Powell, P. Liley, Thermal conductivity of the elements: A comprehensive review, J. Phys. Chem. Ref. Data 3 (1974).
[58] S. Alosious, S.K. Kannam, S.P. Sathian, B. Todd, Prediction of kapitza resistance at fluid-solid interfaces, J. Chem. Phys. 151 (19) (2019) 194502.
[59] C. Niu, H. Lee, S. Chen, Q. Li, J. Du, W. Xu, J.-G. Zhang, M.S. Whittingham, J. Xiao, J. Liu, High-energy lithium metal pouch cells with limited anode swelling and long stable cycles, Nat. Energy 4 (7) (2019) 551–559.
[60] S. Müller, P. Pietsch, B.-E. Brandt, P. Baade, V. de Andrade, F. de Carlo, V. Wood, Quantification and modeling of mechanical degradation in lithium-ion batteries based on nanoscale imaging, Nature Commun. (2018) 2340.
[61] D. Beck, P. Dechent, M. Junker, D.U. Sauer, M. Dubarry, Inhomogeneities and cell-to-cell variations in lithium-ion batteries, a review, Energies 14 (11) (2021) http://dx.doi.org/10.3390/en14113276, URL https://www.mdpi.com/1996-1073/14/11/3276.